

M&MoCS



Shahid Chamran
University of Ahvaz

Journal of Applied and Computational Mechanics



Research Paper

Analysis of Fluid Dynamics and Heat Transfer in a Rectangular Duct with Staggered Baffles

Younes Menni¹, Ahmed Azzi^{1,2}, Ali J. Chamkha^{3,4}, Souad Harmand⁵

¹ Unit of Research on Materials and Renewable Energies, Department of Physics, Faculty of Sciences, Abou Bekr Belkaid University, BP 119-13000-Tlemcen, Algeria

² Department of Mechanical Engineering, Faculty of Technology, Abou Bekr Belkaid University, BP 230-13000-Tlemcen, Algeria

³ Mechanical Engineering Department, Prince Sultan Endowment for Energy and Environment, Prince Mohammad Bin Fahd University Al-Khobar 31952, Saudi Arabia

⁴ RAK Research and Innovation Center, American University of Ras Al Khaimah, United Arab Emirates

⁵ Thermique Ecoulement Mécanique Matériaux Mise en Forme Production - TEMPO - Université de Valenciennes et du Hainaut Cambrésis BP 59313 Valenciennes CEDEX 9, France

Received May 26 2018; Revised June 13 2018; Accepted for publication July 29 2018.

Corresponding author: Y. Menni, menniyounes.cfd@gmail.com

© 2019 Published by Shahid Chamran University of Ahvaz

& International Research Center for Mathematics & Mechanics of Complex Systems (M&MoCS)

Abstract. This computational fluid dynamic analysis attempts to simulate the incompressible steady fluid flow and heat transfer in a solar air channel with wall-mounted baffles. Two 'S'-shaped baffles, having different orientations, i.e., 'S'-upstream and 'S'-downstream, were inserted into the channel and fixed to the top and bottom walls of the channel in a periodically staggered manner to develop vortices to improve the mixing and consequently the heat transfer. The analyses are conducted with the Commercial CFD software FLUENT using the finite volume method for Reynolds number varying from 12,000 to 32,000. The numerical results are presented in terms of streamlines, velocity-magnitude, x -velocity, y -velocity, dynamic pressure coefficient, turbulent kinetic energy, turbulent viscosity, turbulent intensity, temperature field, coefficient and factor of normalized skin friction, local and average numbers of normalized Nusselt, and thermal performance factor. The insertion of the S-shaped baffles in the channel not only causes a much high friction loss, $ff_0 = 3.319 - 32.336$, but also provides a considerable augmentation in the thermal transfer rate in the channel, $Nu/Nu_0 = 1.939 - 4.582$, depending on the S-baffle orientations and the Reynolds number. The S-upstream baffle provides higher friction loss and heat transfer rate than the S-Downstream around 56.443 %, 55.700 %, 54.972 %, 54.289 % and 53.660 %; and 25.011 %, 23.455 %, 21.977 %, 20.626 %, and 19.414 % for $Re = 12,000, 17,000, 22,000, 27,000, \text{ and } 32,000$, respectively. In addition, the result analysis shows that the optimum thermal performance factor is around 1.513 at the highest Reynolds number and S-downstream.

Keywords: Mathematical modelling; Numerical simulation; Heat transfer; Rectangular channel; S-baffles.

1. Introduction

One of the most effective passive strategies of enhancing the convective heat transfer rate in smooth air channels (SAC), such as 'heating [1], cooling [2] or solar [3]' ducts, at 'low [4], moderate [5] or high [6]' Reynolds numbers, is the use of 'attached [7], semi-attached [8] or detached [9]', 'transverse [10] or longitudinal [11]', 'parallel [12], orthogonal [13] or inclined [14]', 'solid [15], perforated [16] or porous [17]', and 'simple [18], corrugated [19] or shaped [20-30]' type obstacles, known as 'vortex generators [31]', 'vortex-flow devices [32]', 'turbulators [33]', 'deflectors [34]', turbulence promoters [35]' or



'disturbances [36]', such as 'ribs [37]', 'fins [38]' or 'baffles [39]', placing on [40] or near [41] the insulated [42] and/or heated [43] channel walls with in-line [44] or staggered manners [45]. This is because the obstacle helps to interrupt the hydrodynamic and thermal boundary layers and to force a vortex downstream [46]. The vortex creates a rotating motion within the flow stream, which causes a rapid transfer of fluid parcels to and from the heat transfer surface [47]. This technique of improvement of the thermal transfer is commonly employed in many various practical engineering and industrial applications such as shell-and-tube heat exchangers with segmental baffle [48], solar energy collectors [49], gas turbine cooling systems [50], and electronic packages [51], therefore, the literature on this topic is widely apparent.

Other similar studies can be found in literature as Ghalambaz et al. [52], Zargartalebi et al. [53], Noghrehabadi et al. [54-57], Sabour et al. [58] and Ghalambaz et al. [59]. In those works, various aspect ratio geometries and various boundary conditions were employed.

Two S-shaped baffles, having different orientation, i.e., S-upstream and S-downstream, were inserted into the channel and fixed to the top and bottom walls of the channel in a periodically staggered manner to develop vortices to improve the mixing and consequently the heat transfer. The suggested shape and orientations were not investigated previously. The present study aims to explore the impact of this design on the phenomenon of thermal transfer inside a constant temperature-surfaced rectangular cross section channel. The Reynolds number is ranged from 12×10^3 to 3.2×10^4 . The analyses are checked through the computational-fluid-dynamic simulations by means of the Commercial CFD software Fluent.

2. Mathematical modelling

Figure 1 depicts a schematic representation of the physical model. Demartini et al. [20] conducted an experimental analysis which served as the basis for the detailed structural parameters used.

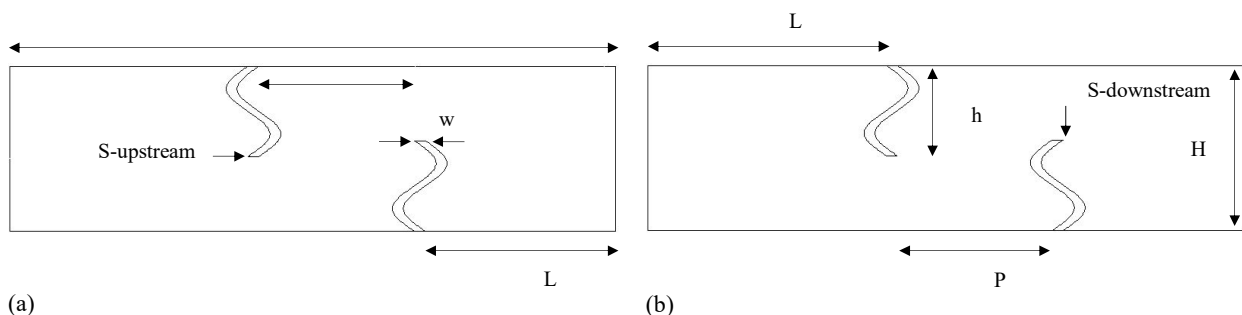


Fig. 1. Channel under study with (a) S-upstream and/or (b) S-downstream baffles.

The computational analysis is performed in a two-dimensional field, which represents a constant temperature-surfaced rectangular cross section channel of $L = 0.554$ m length and $H = 0.146$ m height. Two attached, transverse, orthogonal, solid, S-shape, modern baffles are introduced within the channel; they are arranged on the hot top and bottom channel surfaces in a periodically staggered manner in order to produce vortices which have a substantial influence on the turbulence intensity of the flow, thus causing a larger heat transfer enhancement in the entire domain under investigation. Two various S-baffle orientations are suggested in this analysis, which are referred as cases A and B. In case A, an S-shaped baffle pointed towards the upstream end is considered, called 'S-upstream' (see Fig. 1a) and in case B, an S-shaped baffle pointed towards the downstream end is considered, called 'S-downstream' (see Fig. 1b). The air, whose Prandtl number (Pr) is 0.71, is the working fluid used, and the Reynolds numbers considered range from 12,000 to 32,000.

The computational analysis of fluid dynamics and turbulent forced-convection flow in the whole domain is developed under the following conditions: (i) the steady two-dimensional fluid flow and the thermal transfer, (ii) the constant property incompressible Newtonian fluid, (iii) the body forces and viscous dissipation are ignored, and (iv) the mode of radiation heat transfer is negligible.

Based on the above-mentioned conditions, the mathematical model of the turbulent forced-convection airflow is governed by the Reynolds averaged Navier-Stokes (RANS) equations with the k-epsilon turbulence model [66] and the energy equation. Regarding the Cartesian coordinate, these equations can be written in the following compact form:

$$\frac{\partial}{\partial x}(\rho u \phi) + \frac{\partial}{\partial y}(\rho v \phi) = \frac{\partial}{\partial x} \left[\Gamma_\phi \frac{\partial \phi}{\partial x} \right] + \frac{\partial}{\partial y} \left[\Gamma_\phi \frac{\partial \phi}{\partial y} \right] + S_\phi \tag{1}$$

where ϕ is a vector composed of the scalars $u, v, T, k,$ and ϵ ; u and v stand for the mean velocities towards the x and y axis, respectively; T is the temperature; k and ϵ stand for kinetic energy and turbulent dissipation rate, respectively; Γ_ϕ and S_ϕ represent the turbulent diffusion coefficient and the source term associated with the general variable ϕ in this order. The expressions of ϕ, Γ_ϕ and S_ϕ , are presented for:

Continuity equation

$$\phi = 1 \tag{2a}$$

$$\Gamma_\phi = 0 \tag{2b}$$

$$S_\phi = 0 \tag{2c}$$

Momentum equation in X-direction

$$\phi = u \quad (3a)$$

$$\Gamma_{\phi} = \mu_e \quad (3b)$$

$$S_{\phi} = -\frac{\partial p}{\partial x} + \frac{\partial}{\partial x} \left[\mu_e \left(\frac{\partial u}{\partial x} \right) \right] + \frac{\partial}{\partial y} \left[\mu_e \left(\frac{\partial v}{\partial x} \right) \right] \quad (3c)$$

Momentum equation in Y-direction

$$\phi = v \quad (4a)$$

$$\Gamma_{\phi} = \mu_e \quad (4b)$$

$$S_{\phi} = -\frac{\partial p}{\partial y} + \frac{\partial}{\partial x} \left[\mu_e \left(\frac{\partial u}{\partial y} \right) \right] + \frac{\partial}{\partial y} \left[\mu_e \left(\frac{\partial v}{\partial y} \right) \right] \quad (4c)$$

Energy equation

$$\phi = T \quad (5a)$$

$$\Gamma_{\phi} = \frac{\mu_e}{\sigma_T} \quad (5b)$$

$$S_{\phi} = 0 \quad (5c)$$

k-turbulent kinetic energy equation

$$\phi = k \quad (6a)$$

$$\Gamma_{\phi} = \mu_{\lambda} + \frac{\mu_t}{\sigma_k} \quad (6b)$$

$$S_{\phi} = -\rho \varepsilon + G \quad (6c)$$

ε -turbulent dissipation rate equation

$$\phi = \varepsilon \quad (7a)$$

$$\Gamma_{\phi} = \mu_{\lambda} + \frac{\mu_t}{\sigma_{\varepsilon}} \quad (7b)$$

$$S_{\phi} = (C_{1\varepsilon} f_1 G - C_{2\varepsilon} f_2 \rho \varepsilon) \frac{\varepsilon}{k} \quad (7c)$$

with

$$G = \mu_t \left\{ 2 \left(\frac{\partial u}{\partial x} \right)^2 + 2 \left(\frac{\partial v}{\partial y} \right)^2 + \left(\frac{\partial v}{\partial x} + \frac{\partial u}{\partial y} \right)^2 \right\} \quad (8a)$$

$$\mu_e = \mu_{\lambda} + \mu_t \quad (8b)$$

$$\mu_t = f_{\mu} \rho C_{\mu} \frac{k^2}{\varepsilon} \quad (8c)$$

Where $C_{1\varepsilon} = C_{3\varepsilon} = 1.44$, $C_{2\varepsilon} = 1.92$, $C_{\mu} = 0.09$, $\sigma_k = 1.0$, $\sigma_{\varepsilon} = 1.3$, and $\sigma_T = 0.85$ are the turbulent constants of the model [60].

A uniform one-dimensional velocity profile ($u = U_{in}$) is introduced at the intake of the channel ($x = 0$) while an atmospheric pressure-outlet condition is applied at the exit ($x = L$). No-slip and impermeability boundary conditions are applied over the solid boundaries. A condition of the constant surface temperature of 102°C ($T_w = 375$ K) is applied on the upper and lower walls of the channel. The temperature of air is set equal to 27°C ($T_{in} = 300$ K) at the inlet of the channel. These boundary conditions are presented as

At the intake of the computational domain ($x = 0$)

$$u = U_{in} \quad (9a)$$

$$v = 0 \quad (9b)$$

$$T = T_{in} \quad (9c)$$

$$k_{in} = 0.005 U_{in}^2 \quad (9d)$$

$$\varepsilon_{in} = 0.1 k_{in}^2 \quad (9e)$$

At the channel walls (upper wall: $y = H/2$; lower wall: $y = -H/2$)

$$u = v = 0 \quad (10a)$$

$$k = \varepsilon = 0 \quad (10b)$$

$$T = T_w \quad (10c)$$

At the fluid/solid interface

$$T_f = T_s \quad (11a)$$

$$\lambda_f \frac{\partial T_f}{\partial n} = \lambda_s \frac{\partial T_s}{\partial n} \tag{11b}$$

Where n is the normal coordinate to the wall.

At the exit ($x = L$)

$$\frac{\partial u}{\partial x} = \frac{\partial v}{\partial x} = \frac{\partial T}{\partial x} = \frac{\partial k}{\partial x} = \frac{\partial \varepsilon}{\partial x} = 0 \tag{12a}$$

$$P = P_{atm} \tag{12b}$$

The flow Reynolds number (Re) based on the channel aeraulic diameter,

$$D_h = 2HW / (H + W) , \tag{13a}$$

is given by

$$Re = \rho \bar{U} D_h / \mu \tag{13b}$$

The skin friction coefficient (Cf) is given by

$$Cf = \frac{\tau_w}{\frac{1}{2} \rho \bar{U}^2} \tag{14a}$$

The friction factor (f) is evaluated from the pressure drop (ΔP) as

$$f = \frac{(\Delta P / L) D_h}{\frac{1}{2} \rho \bar{U}^2} \tag{14b}$$

where \bar{U} presents the average axial velocity of the section and τ_w is the shear stress to the wall. To determine the heat transfer rate inside the channel, the heat transfer is measured by the local Nusselt number (Nu_x) which can be written as

$$Nu_x = \frac{h_x D_h}{k_f} \tag{15a}$$

and the average Nusselt number (Nu) can be obtained by

$$Nu = \frac{1}{L} \int Nu_x \partial x \tag{15b}$$

The following expression represents the thermal enhancement factor (TEF):

$$TEF = (Nu / Nu_0) / (f / f_0)^{1/3} \tag{16}$$

The Dittus-Boelter and Petukhov correlations [61] can be used to normalize the average Nusselt number and the friction factor, respectively. The quantities Nu_0 and f_0 are the average Nusselt number and the friction factor of the smooth channel, respectively. The Dittus and Boelter correlation has the following form:

$$Nu_0 = 0.023 Re^{0.8} Pr^{0.4} \text{ for } Re \geq 10^4 \tag{17a}$$

The Petukhov correlation has the following form:

$$f_0 = (0.79 \ln Re - 1.64)^{-2} \text{ for } 3 \times 10^3 \leq Re \leq 5 \times 10^6 \tag{17b}$$

3. Numerical simulation

The Commercial CFD software FLUENT is used to simulate the incompressible steady fluid flow and heat transfer in the computational model. The governing flow equations are integrated by the Finite Volume Method (FVM), details of which can be found in Patankar [62]. The QUICK numerical scheme, developed by Leonard and Mokhtari [63], is employed to discretize the convective terms. The SIMPLE discretization algorithm is used for the pressure velocity.

To control the update of the computed variables at each iteration, the under-relaxation was varied between 0.3 and 1.0 (Nasiruddin and Kamran Siddiqui [47]). The under-relaxation factor is carefully chosen to prevent large variations in the source terms. The solution is assumed to be converged when the following criterion is satisfied:

$$Max \left(\frac{|\phi - \phi^*|}{|\phi^*|} \right) \leq \delta \tag{18}$$

where ϕ^* denote the previews iteration value and δ is a prescribed error. For the present simulation, $\delta = 10^{-9}$ for $\phi \equiv (u, v, k, \varepsilon)$ and $\delta = 10^{-12}$ for $\phi \equiv (T)$ are selected.

A quadrilateral-type structured grid in the two-directions is inserted. The grid independence tests are performed by realizing CFD simulations in the whole domain investigated with S-shaped baffles, using different grid systems with the number of mesh nodes ranging from 35 to 145 along the pipe depth and 95 to 370 along the length. The grid system with the number of nodes equal to 245×95 (in X and Y directions respectively) performs around 0.330 %, and 0.372 % deviation for the Nu and f , respectively, compared with the grid of size 370×145 . Therefore, the grid cell of 245×95 is selected for the rest of the study.

The precision of the computational fluid dynamic software and the correctness of the numerical approach conducted are verified. For a rectangular air channel with simple flat rectangular obstacles, the distributions of the axial profiles of speed and

the pressure coefficient along the depth of the channel are followed and shown in Fig. 2 (a) and (b), respectively. These numerical results are validated with the numerical and experimental results of Demartini et al. [20] for the same structural condition under similar operating parameters. As shown on these plots, a good agreement is obtained.

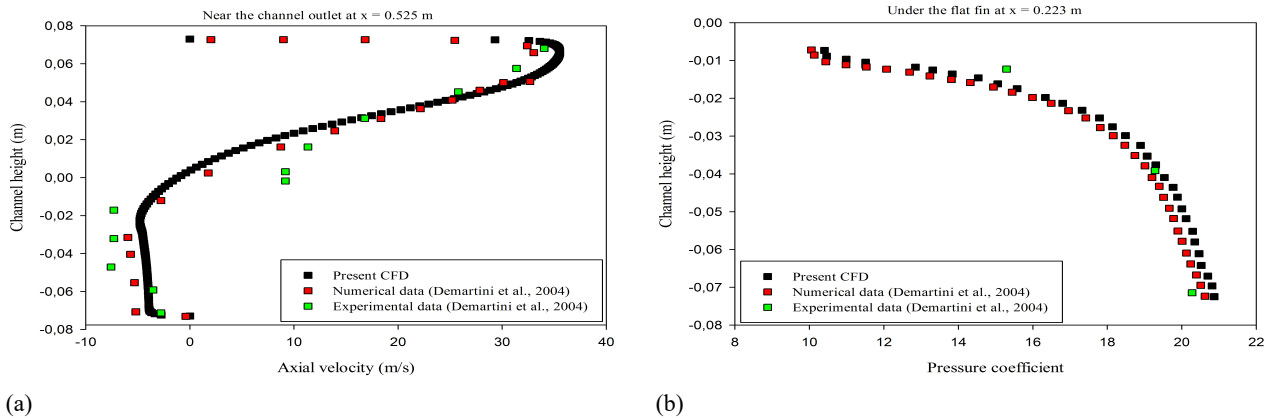


Fig. 2. Numerical validation of (a) axial velocity and (b) pressure coefficient for $Re = 8.73 \times 10^4$.

The evolutions of the Nusselt number and the friction factor as a function of the Reynolds number are also simulated for a smooth air channel and compared with the empirical correlation of Dittus-Boelter and Petukhov, as shown in Fig. 3 (a) and (b), respectively.

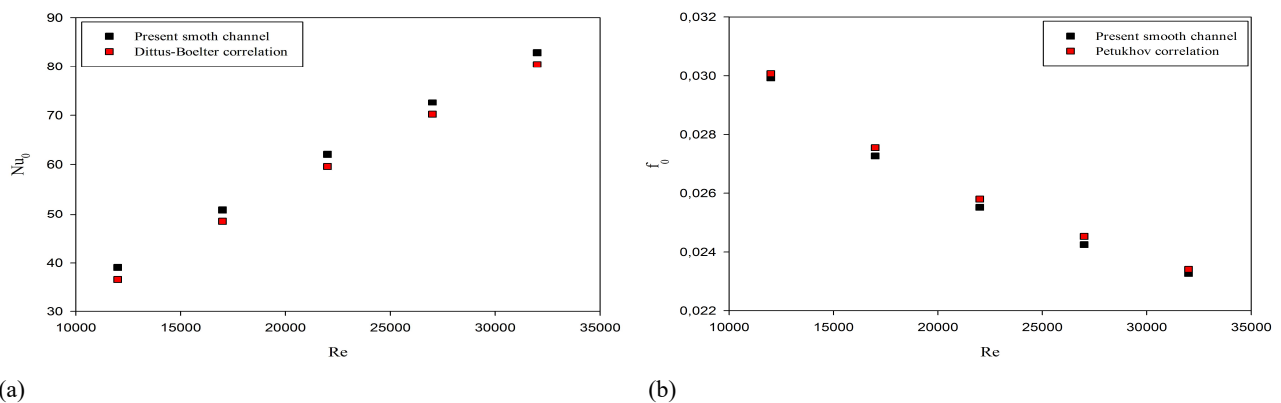


Fig. 3. Numerical verification of (a) Nusselt number and (b) friction factor for smooth channel with no baffle.

As can be shown in Fig. 3, the present smooth channel results agree well with the available correlations with $\pm 3.5\%$ in comparison with Dittus-Boelter correlation (1930) for the Nu_0 and $\pm 1.15\%$ in comparison with Petukhov correlation (1970) for f_0 .

4. Results and discussion

4.1. Streamlines

Figure 4 (a), (b), (c), (d), and (e) shows the contour plots of streamlines for the S-upstream and S-downstream cases with $Re = 12,000, 17,000, 22,000, 27,000,$ and $32,000$, respectively. In both S-baffle cases, the plots reveal the existence of three main regions. In the first region, just the upstream of the S-baffles, the fluid is accelerated and arrives with an axial speed. At the approach of the S-baffles, the current lines are deflected. In the second region, located between the top of each S-baffle and the walls of the channel, the flow is accelerated due to the effect of cross-sectional reduction.

In the third region, the downstream of the S-baffles, the current lines are generated by the effect of flow expansion, thus leaving the section formed by the S-baffles and the walls. The most important phenomenon occurring in this zone is the formation of a recirculating flow whose extent is proportional to the Reynolds number. The S-upstream baffle provides higher stream-function value than the S-downstream around 14.742 %, 14.798 %, 14.805 %, 14.752 %, and 14.720 % for $Re = 12,000, 17,000, 22,000, 27,000$ and $32,000$, respectively.

4.2. Velocity-magnitude

The mean velocity fields in the whole domain examined are presented in Fig. 5 (a), (b), (c), (d), and (e) for cases $Re = 12,0$

00, 17,000, 22,000, 27,000, and 32,000, respectively. Both the cases of the S-baffle are also presented.

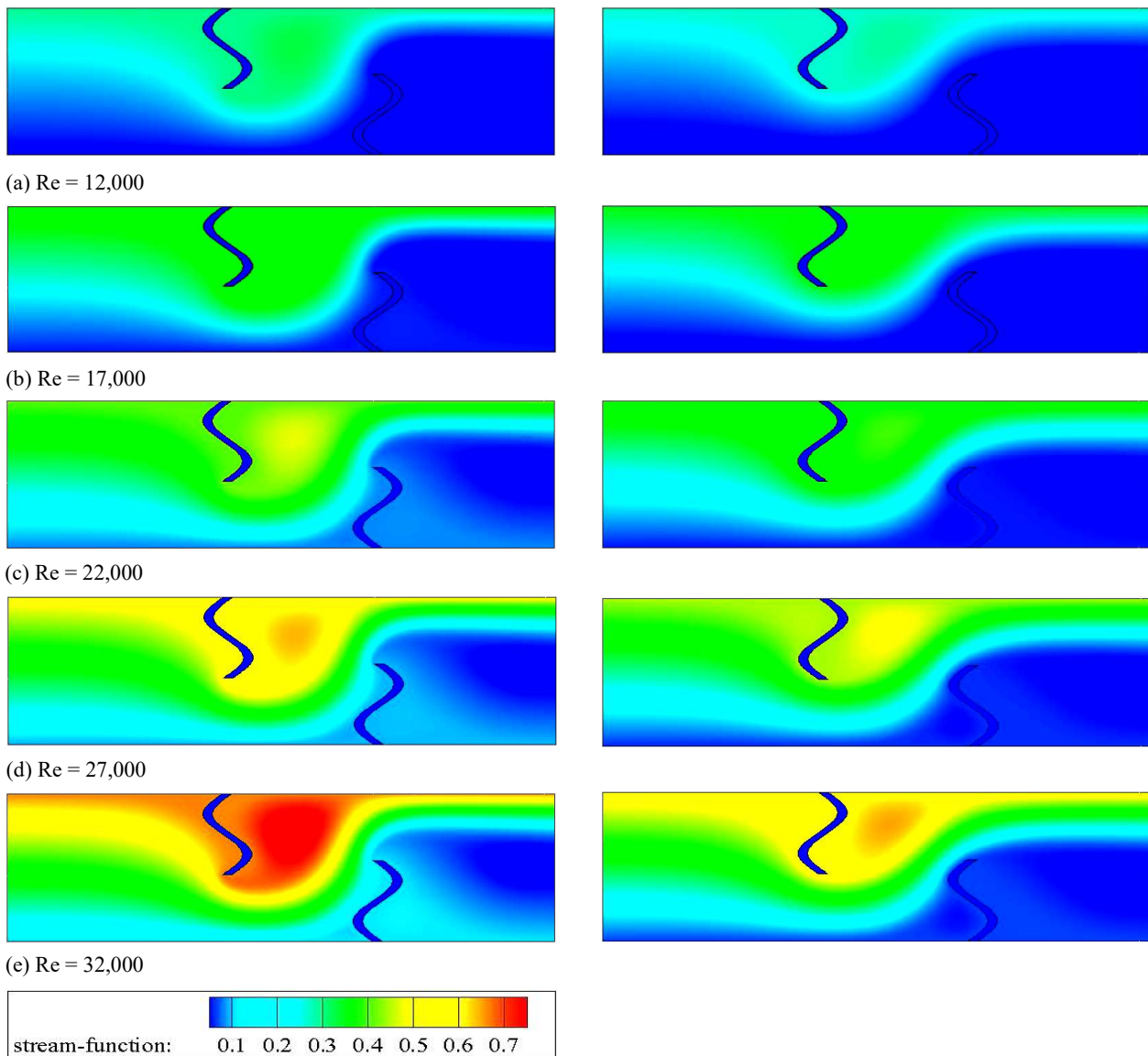


Fig. 4. Streamlines for S-upstream and S-downstream cases as a function of Reynolds number. Stream-function values in kg/s.

It can clearly be noticed that the values of the fluid velocity are very low in the vicinity of the two S-baffles, especially in the downstream regions; this is due to the presence of the recirculation zones. Far from these zones, the current lines become parallel, which results in the progressive development of the flow. One should also note that the velocity increases in the space between the end of each S-baffle and the wall of the channel. This rise in the velocity is generated first by the presence of the S-baffle and then by the presence of a recycling which results in a sudden change in the direction of the flow. It is also observed that the highest values of the velocity appear near the top of the channel, with an acceleration process that begins just after the second S-baffle. From the figure, it can clearly be seen that the velocity is proportional to the Reynolds number, for both the cases under study.

4.3. X-Velocity

Figure 6 shows the axial velocity contour plots for the flow of air in the channel for two different S-baffle orientations (S-upstream and S-downstream). In the figure, the axial velocity is related as a function of Reynolds number ($Re = 12,000, 17,000, 22,000, 27,000,$ and $32,000$). Note that the presence of the first S-baffle in the upper half of the channel induces a strong decrease in the axial velocity. Negative velocities indicate the presence of a small recirculation zone located upstream of this same baffle, paradoxically in the lower half, where the flow increases, and particularly in the vicinity of the passage under the S-baffle.

As the velocity contour plots, the S-upstream baffles perform a greater fluid velocity than the S-downstream. Downstream of this same first S-baffle, two large distinct zones can be quantified, as presented in Fig. 6. The first one is an area where the fluid particles follow the main flow direction.

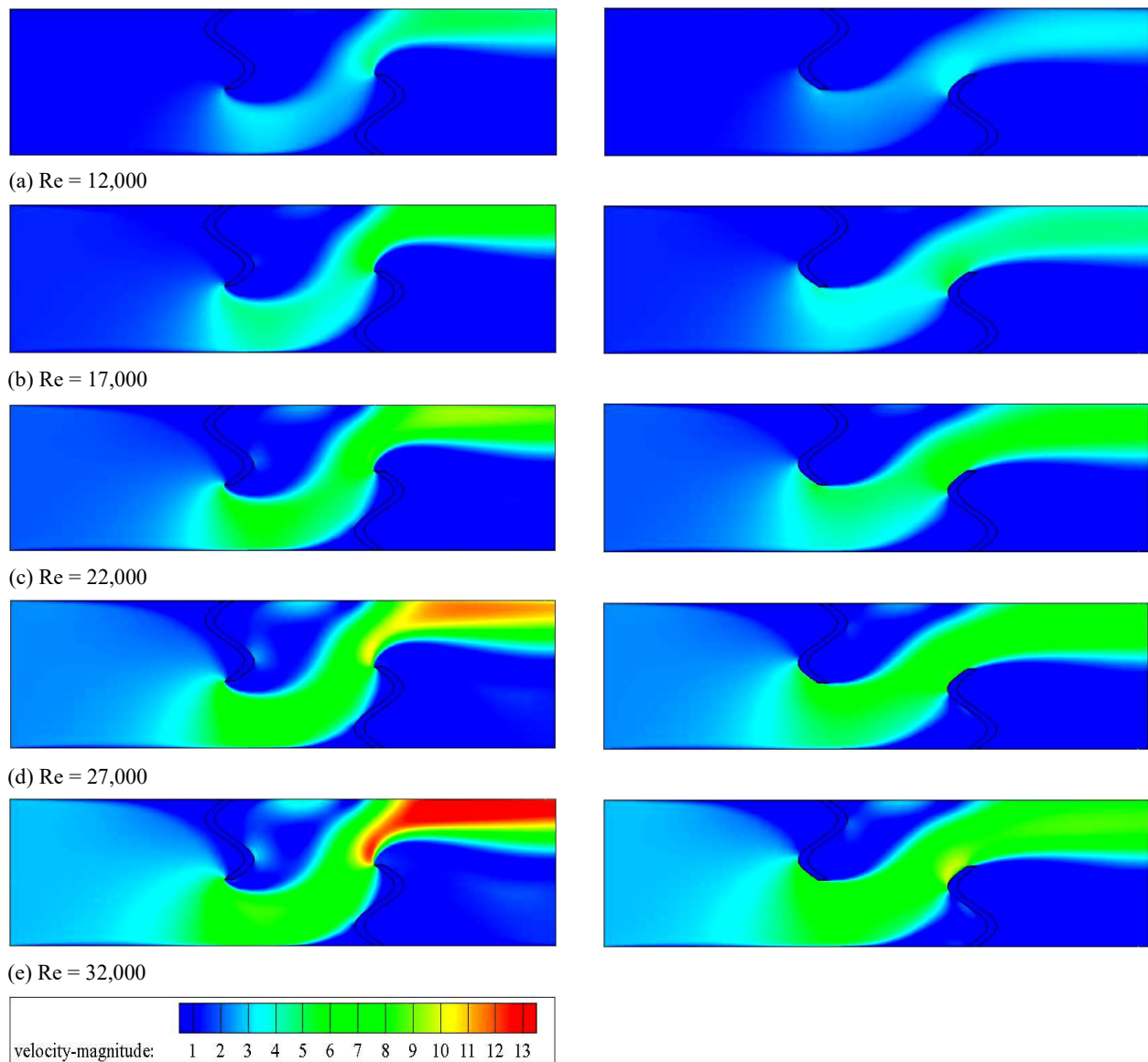


Fig. 5. Velocity-magnitude fields for S-upstream and S-downstream cases as a function of Reynolds number. Velocity-magnitude values in m/s.

The recirculation zone is located in the second region in the vicinity of the upper right S-baffle face. The flow is reversed and this causes the flow to peel off at the top wall of the channel; the velocity profiles are directed in the way opposite to that of the flow. Upstream of the second S-baffle, note that the flow velocity, when approaching the S-baffle, is reduced in the lower part of the canal, whereas in the upper part, the flow begins to accelerate towards this breach above the second S-baffle. This limitation depends substantially on the recirculation zones, which are characterized by negative values and are located upstream and downstream of the second S-baffle. The vortices occur in the vicinity of these zones; they develop and increase the resistance to the flow very strongly. These disordered but localized movements are characterized by negative values, as shown in Fig. 6.

Downstream and according to the results in Fig. 6, the speed value reaches approximately 13.850 m/s, which is 13.195 times greater than the velocity at the inlet. These values can be reached only because of the very high recirculation to the rear of the second obstacle. The increase in the Reynolds number leads to an acceleration of the flow and causes a rise in the fluid x-velocity, indicating that the length of the vortices is proportional to the augmentation in the Re number (see Fig. 4) which characterizes the flow. In addition, the plots show that the S-downstream baffle has smaller x-velocity values than those of the S-upstream baffle, regardless of the number of Reynolds. These same plots also indicate that the x-velocities, for both S-baffle models, increase significantly as the number of Reynolds number.

4.4. Y-Velocity

As for the transverse component of the velocity, it is interesting to note that for both cases studied, the negative velocity gradients are observed at the top of the upper wall-mounted S-baffle and positive velocity gradients at the top of the lower wall-mounted S-baffle (Fig. 7).

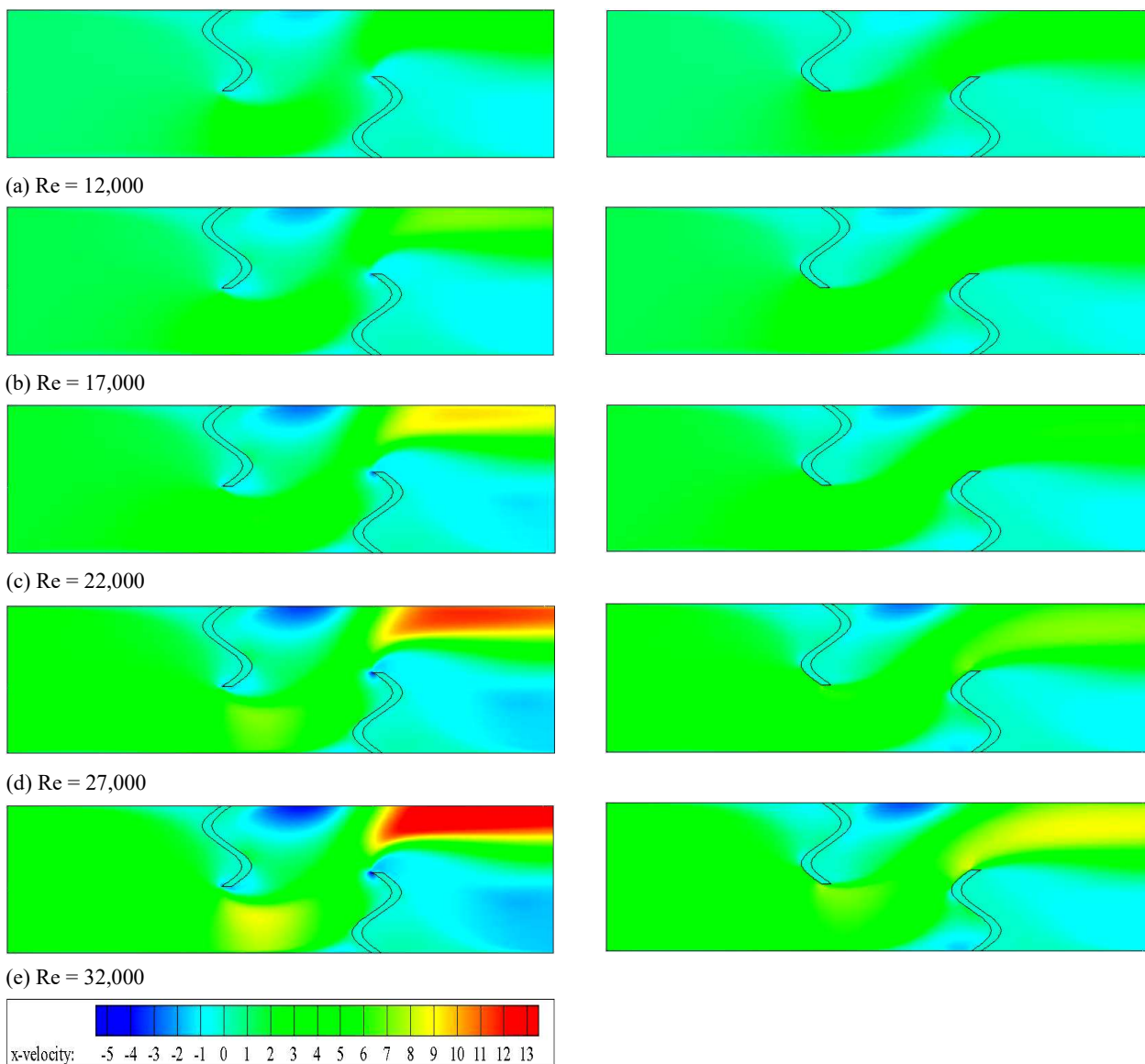


Fig. 6. X-velocity fields for S-upstream and S-downstream cases as a function of Reynolds number. X-velocity values in m/s.

In the figure, the y-velocity values are also related as a function of Reynolds number. It is seen that the y-velocity augments with augmenting Reynolds number in both cases and in general, the maximum y-velocity is obtained for S-upstream while the lowest one is for S-downstream.

4.5. Dynamic pressure

To follow more precisely the evolution of fluid flow into the airway, the contour plots of dynamic pressure fields are added as listed below in Fig. 8 (a)-(e). As illustrated in this figure and similar to the results in Fig. 5 (a)-(e) of the speed fields, the pressure values are very low next to the S-baffles, especially in the back areas, because of the existence of recirculation cells. In areas confined between the upper sides of the S-baffles and the inner walls of the channel, the pressure values increase. The coefficients of dynamic pressure are maximal next to the upper surface of the airway near the exit, also near the top left side of the lower wall-mounted S-baffle, due to the high speed of air flow in these regions. In the figure, it is interesting to note that the dynamic pressure value tends to augment with the rise of Reynolds number values for both treated S-baffle cases. The use of S-upstream baffle performs much better than that of S-downstream baffle for the enhanced y-velocity.

4.6. Turbulent kinetic energy

The contour plots of turbulent kinetic energy fields obtained under turbulent flow regime for both S-baffle configurations with five various values of Reynolds number, $Re = 12,000, 17,000, 22,000, 27,000,$ and $32,000$ are presented in Fig. 9 (a) to (e), respectively. The trends of turbulent kinetic energy are similar for both cases under investigation.

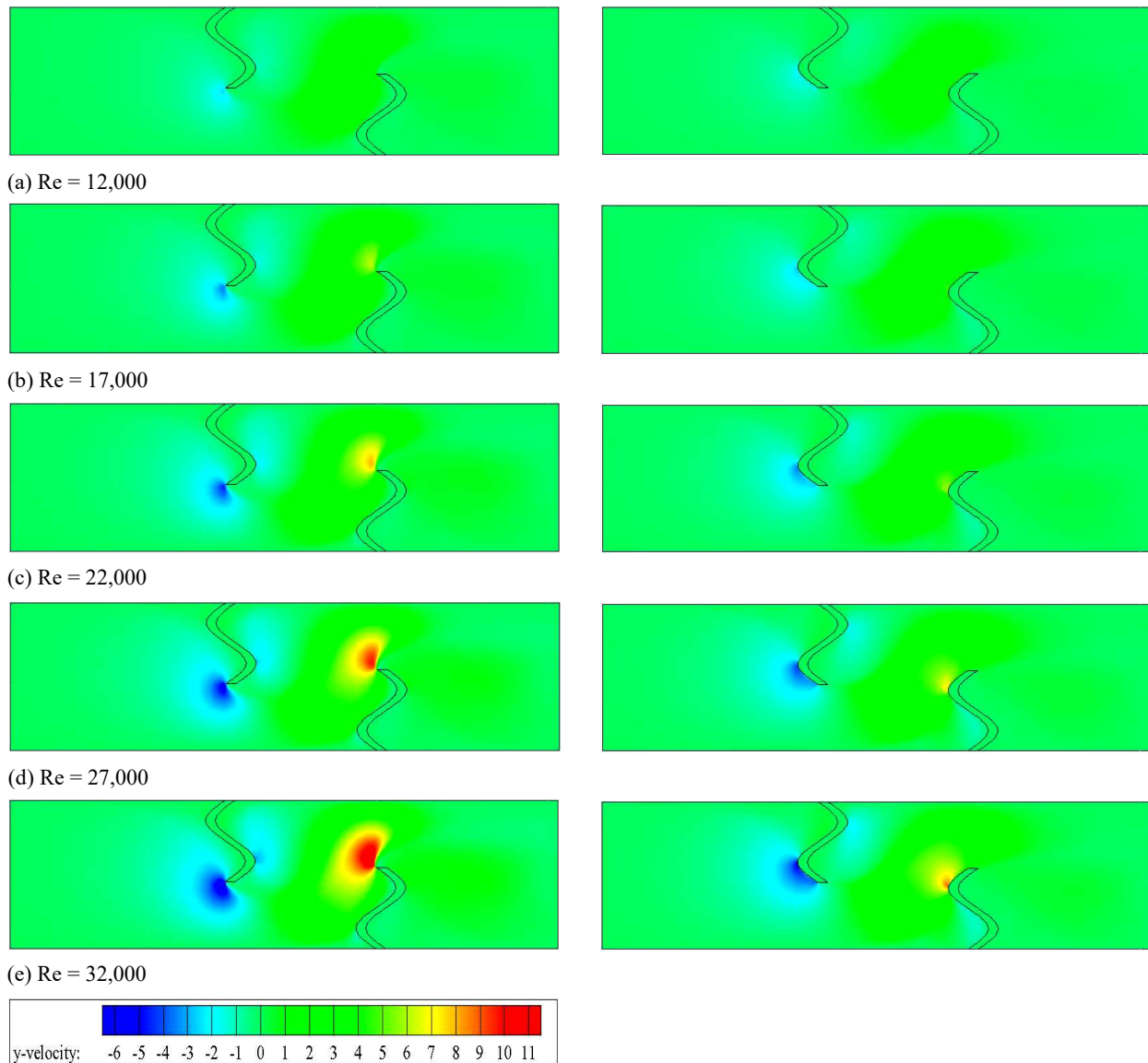


Fig. 7. Y-velocity fields for S-upstream and S-downstream cases as a function of Reynolds number. Y-velocity values in m/s.

The plots show the largest value in the region opposite the right S-baffle and the smallest value in the region around the left S-baffle for both the S-upstream and S-downstream simulated. The turbulent kinetic energy augments with the augmentation of the Reynolds number (Re), and consequently, the $Re = 32,000$ provides the maximum turbulent kinetic energy in both cases studied. The use of S-upstream baffle shows better turbulent kinetic energy distribution values over the S-downstream baffle at almost stations.

4.7. Turbulent viscosity

The distributions of turbulent viscosity in the whole domain reported for two different S-baffle models (S-upstream and S-downstream) at different Reynolds numbers, $Re = 12,000$, $17,000$, $22,000$, $27,000$, and $32,000$ are shown in Fig. 10 (a) to (e), respectively. Similar to the results in Fig. 9 (a) to (e), the largest variations in the turbulent viscosity are found in the regions opposite the lower wall-attached S-baffle, due to the high velocities in those regions. In addition, it is interesting to note that the value of the turbulent viscosity tends to augment with the rise of Reynolds number values for both models of the S-baffle. However, it is worth noting that for all Reynolds numbers employed, the model of S-upstream provides the highest turbulent viscosity value.

4.8. Turbulent intensity

The effect of changing S-baffle shape geometries on the flow structure in terms of turbulent intensity for the channel with S-upstream and/or S-downstream at different flow rate values, $Re = 12,000$, $17,000$, $22,000$, $27,000$, and $32,000$, is represented in Fig. 11 (a) to (e). In Fig. 11, the turbulent intensity tends to augment with the increase of the Reynolds number for the two cases simulated. The upper turbulent intensity values near the tip of the second S-baffle are due to the high velocities in that region. However, it is worth noting that for both S-baffle configurations investigated, the S-upstream configuration provides

the highest turbulent intensity value.

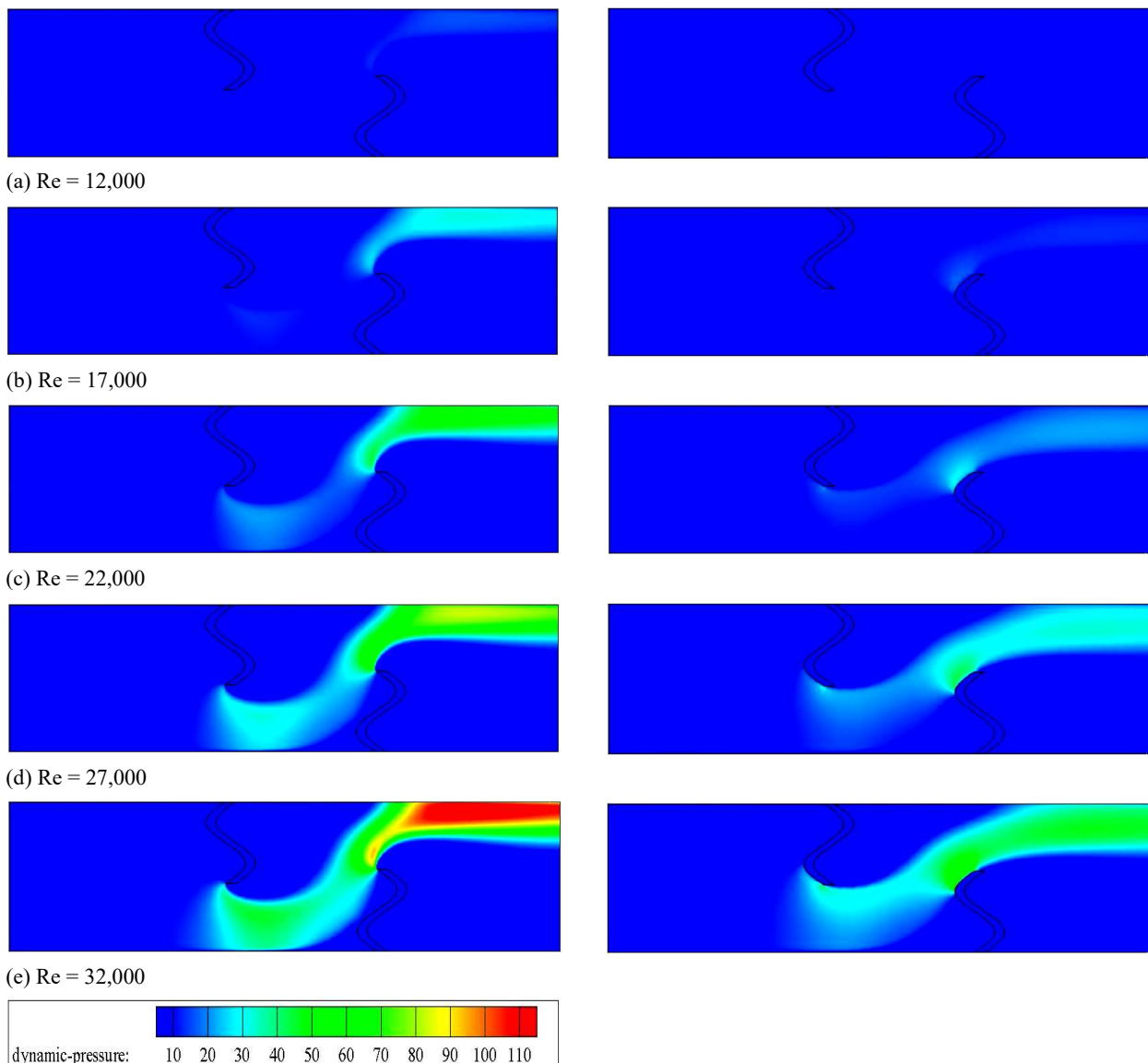


Fig. 8. Dynamic pressure fields for S-upstream and S-downstream cases as a function of Reynolds number. Dynamic pressure values in Pa.

4.9. Temperature field

Figure 12 depicts the contour lines of temperature in the entire region under study for the cases of various S-baffle configurations treated. One can easily note in Fig. 12 that the temperature changes significantly over the hot walls of the channel for both S-baffle cases investigated. This suggests that the temperature field is considerably influenced by the recirculation flows as it can cause better mixing of the fluid in the area between the hot surfaces and the core flow regions. This should result in a high-temperature gradient over the hot surfaces. These observations are confirmed by Sripattanapipat and Promvongse [46]. The temperature field shown also indicates a temperature drop in the regions situated between the end of each S-baffle and the hot walls of the channel, with an acceleration process that begins just after the first and the second S-baffles. Therefore, there is an inverse proportionality between the increase in the flow velocity and the temperature of the fluid in each cross section of the channel. Moreover, based on the analysis of the numerical results of the velocity fields (see Fig. 4), as well as that of the temperature fields (see Fig. 12), for different S-baffle models used, a relation exists between the fluid temperature and the flow velocity.

4.10. Normalized local and average Nusselt numbers

The local Nusselt number (Nu_x) for cases S-upstream and S-downstream normalized by the Nusselt number (Nu_0) of the case of smooth air channel with no baffle is shown in Fig. 13 as a function of the hot upper channel wall length at different Reynolds numbers of 12,000, 17,000, 22,000, 27,000, and 32,000.

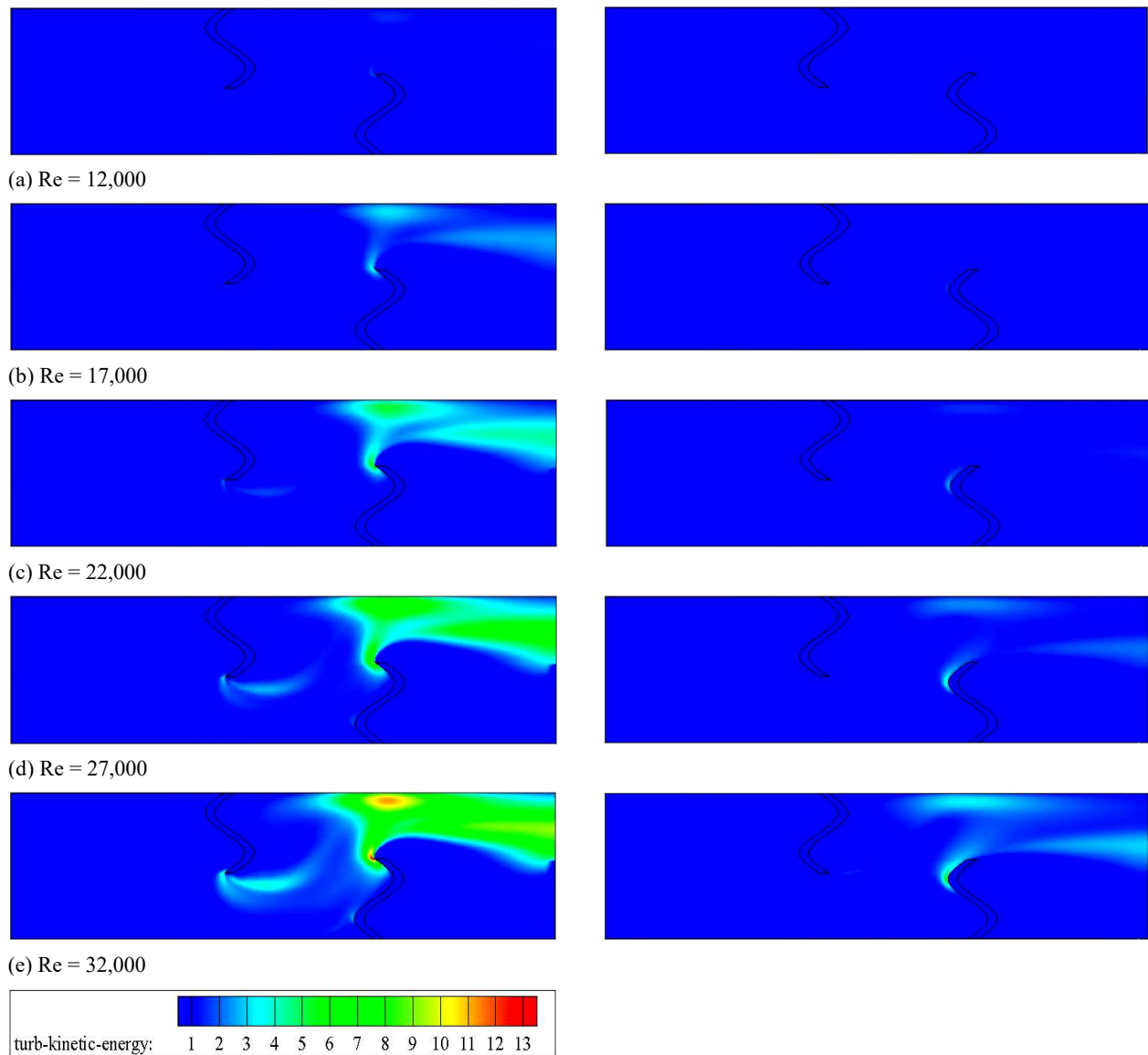


Fig. 9. Turbulent kinetic energy fields for S-upstream and S-downstream cases as a function of Reynolds number. Dynamic pressure values in m^2/s^2 .

The local Nusselt number is minimal in the region around the first S-obstacle; it is maximal in the region opposite to the second S-obstacle, which is the case of the configuration under study. In the intermediate zone, significant values are found due to the recirculation of the fluid downstream of the first S-obstacle. The results obtained are in a good agreement with those of all the studies which assert that locally some recirculation zones appear and this corresponds to a greater transfer of heat (for example, see Nasiruddin and Kamran Siddiqui [47]). Upstream of the first S-obstacle, low values are found; this is due to the change in the direction of flow caused by this same obstacle towards the lower part of the channel with high velocities. The local Nusselt number is also affected by the Reynolds number. A linear increment exists between the local Nusselt number and the Reynolds number for both the S-baffle case treated. The figure also shows that the S-baffle model has a significant impact on the local the heat transfer rate. As expected, the Nu_x/Nu_0 ratio obtained from the S-upstream baffle is substantially higher than that from the S-downstream one for all Reynolds number used.

Figure 14 shows the variations of the normalized average Nusselt number (Nu/Nu_0) with the flow rate in terms of the Re number at different cases for the channel with the S-shaped baffles. In the figure, the Nu/Nu_0 rate tends to augment with the augmentation of the Re value from 12,000 to 32,000 for all S-models. The baffle in S-upstream case provides upper Nu/Nu_0 ratio than the one in S-downstream case around 25.011 %, 23.455 %, 21.977 %, 20.626 %, and 19.414 % for $\text{Re}=12,000$, 17,000, 22,000, 27,000, and 32,000, respectively. In both S-baffle cases, the baffled duct airflows give upper Nu values than that for smooth rectangular duct air flow due to the induction of high re-circulation in the baffled duct, leading to upper gradients of temperature. In the range under study, the normalized average Nusselt number is found around 1.939 - 4.582, depending on S-baffle orientations and Reynolds number. The value of Nu is around 2.586, 3.231, 3.759, 4.203, and 4.582 times upper than the smooth rectangular duct in the absence of baffles and fins for $\text{Re} = 12,000$, 17,000, 22,000, 27,000, and 32,000, respectively, for the case of S-upstream, while around 1.939, 2.473, 2.933, 3.336, and 3.692 times for the case of S-downstream.

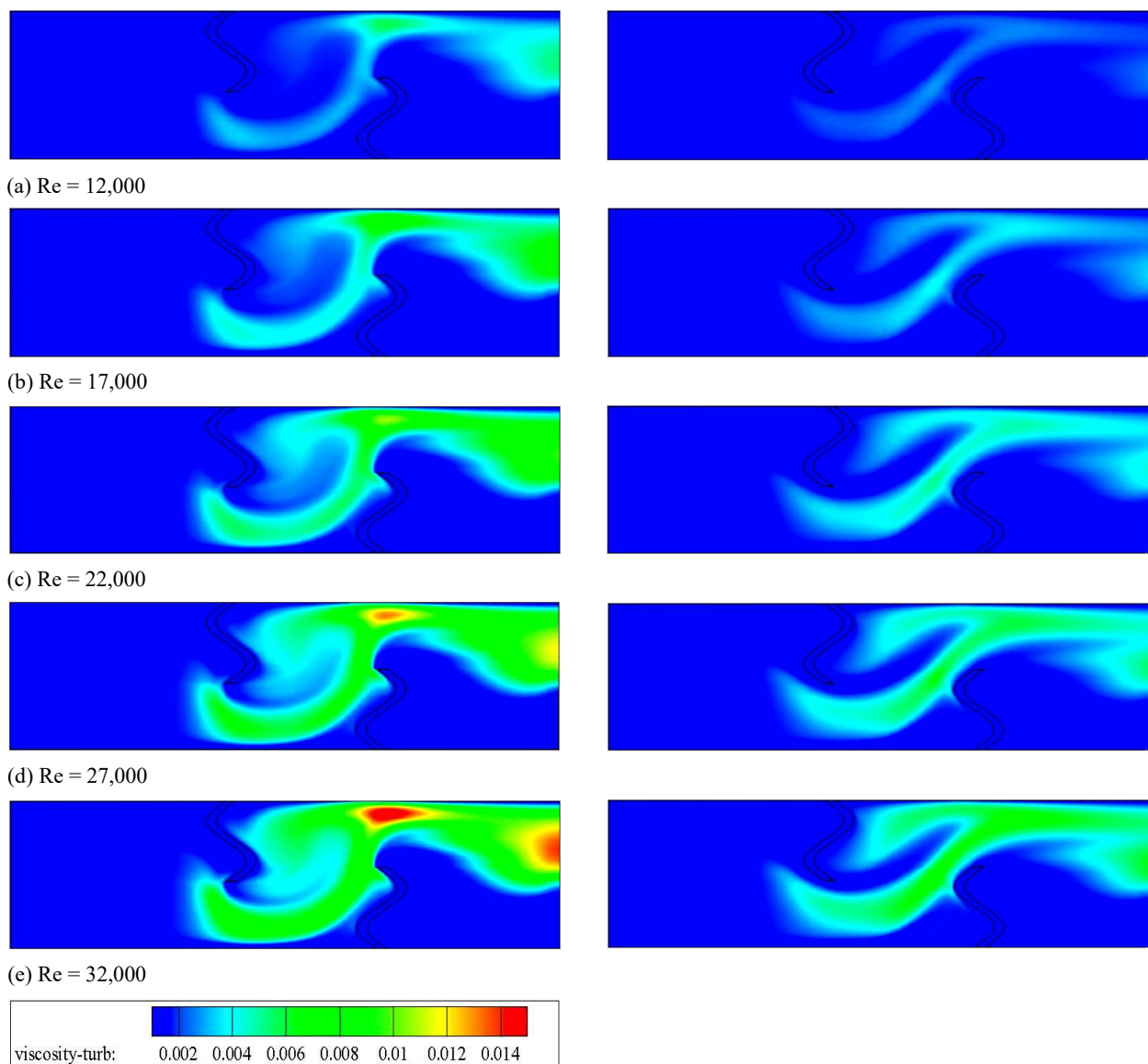


Fig. 10. Turbulent viscosity fields for S-upstream and S-downstream cases as a function of Reynolds number. Turbulent viscosity values in Kg/m-s.

4.11. Normalized local and average friction coefficients

By and large, the increase in heat transfer is not enhanced by the rise of the coefficient of skin friction, as this would lead to a larger pressure decline. Equation (14a) may be used to determine the distribution of the skin friction coefficient. Figure 15 depicts the skin friction coefficient, C_f , along the upper channel wall for different Reynolds number values in the cases of different S-baffles, i.e., S-upstream and S-downstream. This same figure shows that the increase in the coefficients of skin friction is more significant than the one of the coefficients of heat transfer generated by the temperature field. This may suggest that the velocity and turbulence fields grow faster than the isotherms. Both S-configurations give the same trends of the skin friction coefficient (C_f). The smallest skin friction coefficient is found around the first S-baffle; the largest one is encountered in the region facing the second S-baffle, which represents the situation of the configuration under study.

Note that at the starting out of the test section, the coefficient of skin friction decreases significantly because of the first S-baffle that is placed in the top part of the channel. In this case, the air has the possibility to flow in the direction of the bottom surface, and as a result, the contact between air and the upper wall of the channel is negligible. Nevertheless, the skin friction coefficients are larger again at the positions corresponding to the flow recirculation areas, as displayed in the figure. The S-baffles placed on the top and bottom walls cause the flow direction to change, and consequently, the largest values of the skin friction coefficient come out in the recirculation region after the second S-baffle.

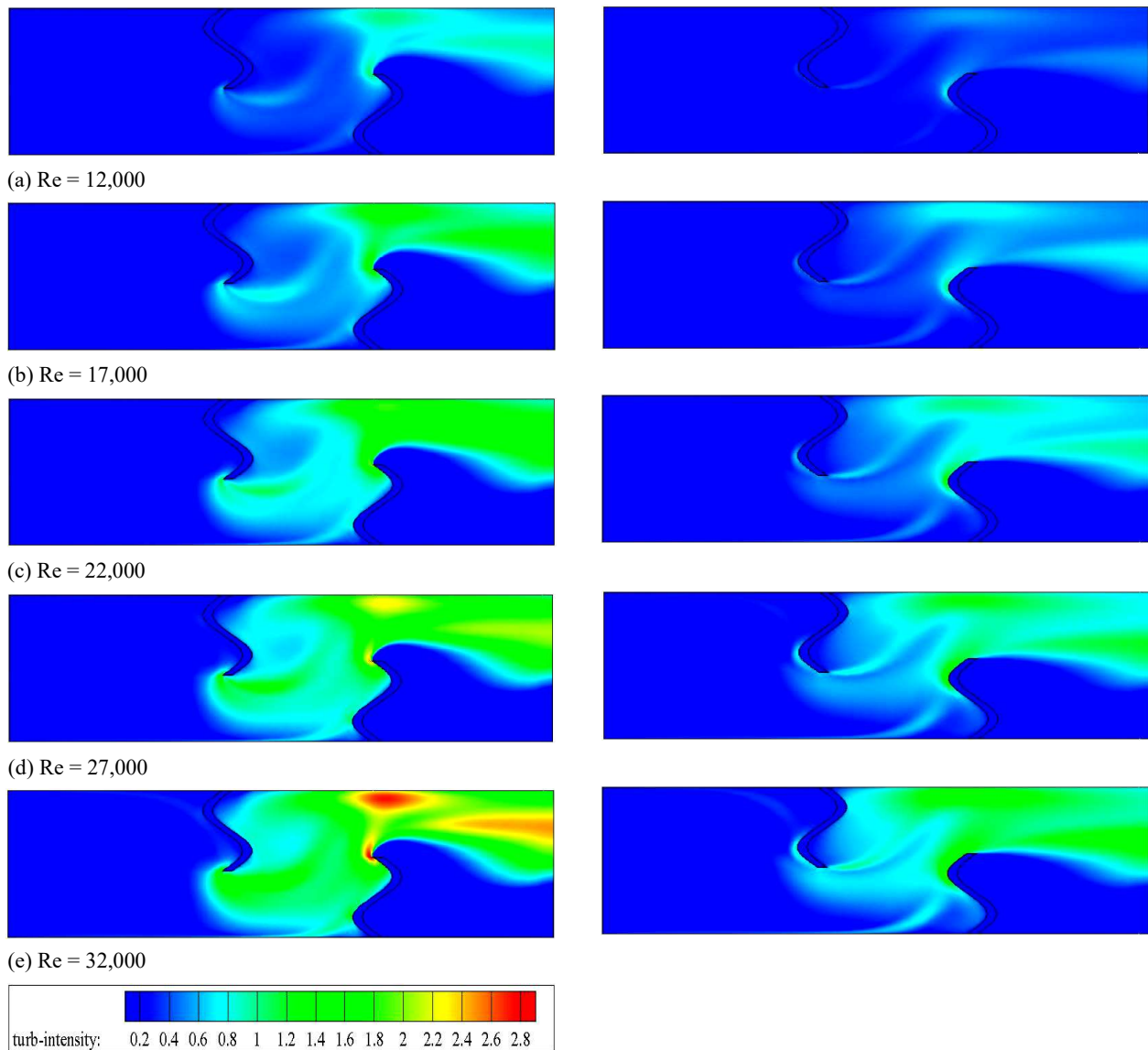


Fig. 11. Turbulent intensity fields for S-upstream and S-downstream cases as a function of Reynolds number. Turbulent intensity values in $100 \times \%$.

It is worth mentioning that an acceleration process begins right after the first and the second S-baffles. As the figure shows, the S-upstream performs greater skin friction coefficient than the S-downstream for all Re numbers applied. The comparison of the results in the same figure indicates that the S-baffle orientation has an impact on the friction loss. For the case B, the S-baffle orientation is towards the downstream side, therefore, it causes less distortion of the flow, especially at lower values of Re number. Whereas, for the case A, the S-baffle orientation is towards the upstream side which causes significantly large flow distortion, where the effect of Re number is very significant. The Reynolds number also affects the skin friction coefficient. It is admitted that in both A and B cases, when the Reynolds number increases, the skin friction loss becomes more important.

Figure 16 shows the variations of the normalized friction factor (ff_0) with the Reynolds number at various S-baffle orientations. In general, the ff_0 value augments with augmenting the Reynolds number. The friction loss of S-downstream baffle is lower than that of S-upstream baffles, which indicates that the S-downstream is more advantageous than the other. At Reynolds numbers of 12,000, 17,000, 22,000, 27,000, and 32,000, the S-downstream baffles seemed to decrease the ff_0 ratio by about 56.443 %, 55.700 %, 54.972 %, 54.289 %, and 53.660 % relative to the S-upstream baffles, respectively. The augmentation in the friction factor (f) for the S-baffles with both orientations is much higher than that for the smooth rectangular air channel. The factor of friction is around 7.621 - 32.336 and 3.319 - 14.984 times above the smooth rectangular channel for the S-upstream and S-downstream, respectively.

4.12. Thermal aerodynamic performances

Figure 17 shows the evolution of the thermal enhancement factor (TEF), calculated by Equation (16), as a function of Reynolds number ($Re = 12,000, 17,000, 22,000, 27,000,$ and $32,000$) with a constant section of the channel for the lower surface of the hot upper wall of the channel. As expected, the thermal enhancement factor increases with the increase in the Reynolds number in both studied cases (S-upstream and S-downstream).

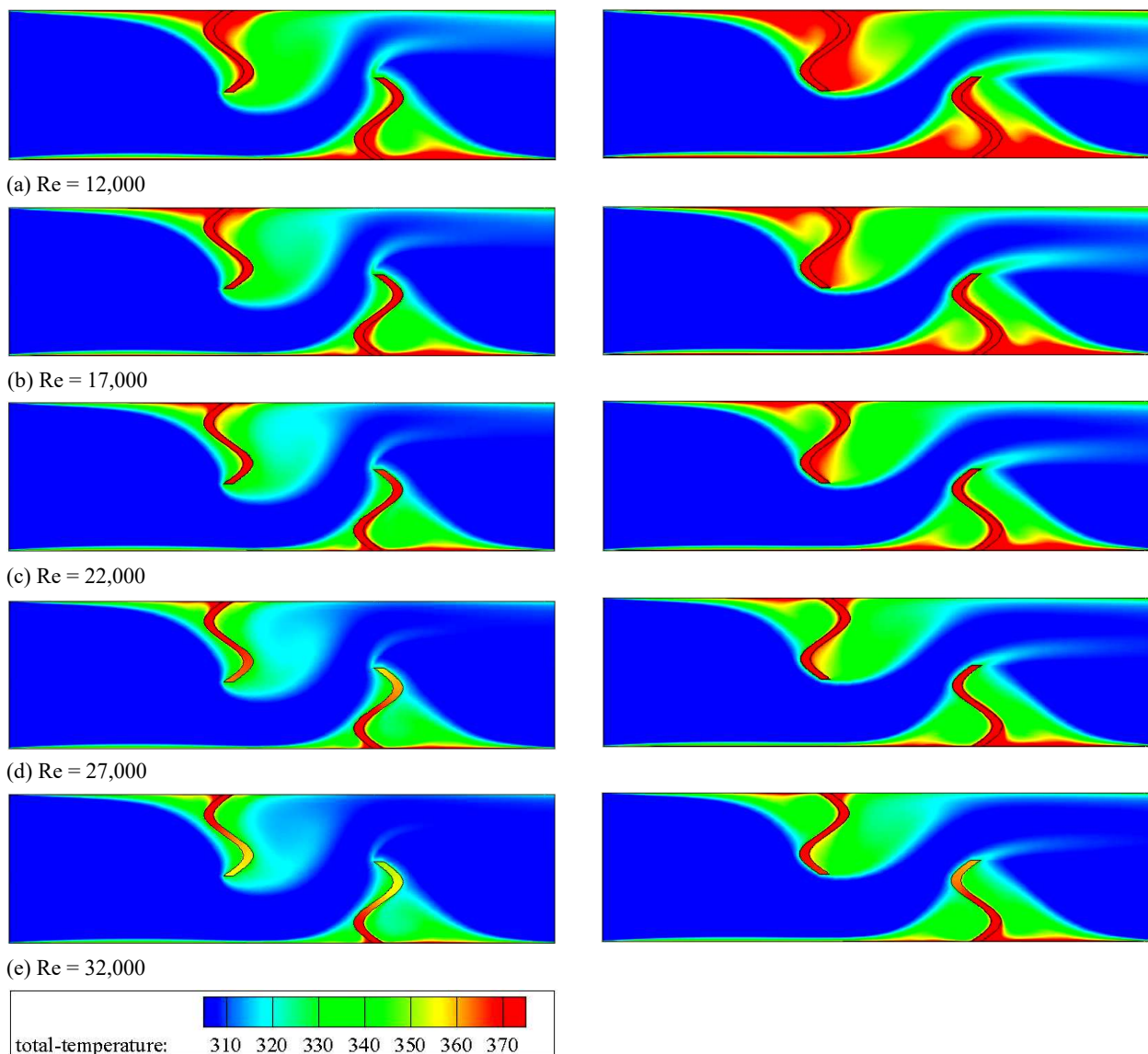


Fig. 12. Temperature fields for S-upstream and S-downstream cases as a function of Reynolds number. Temperature values in K.

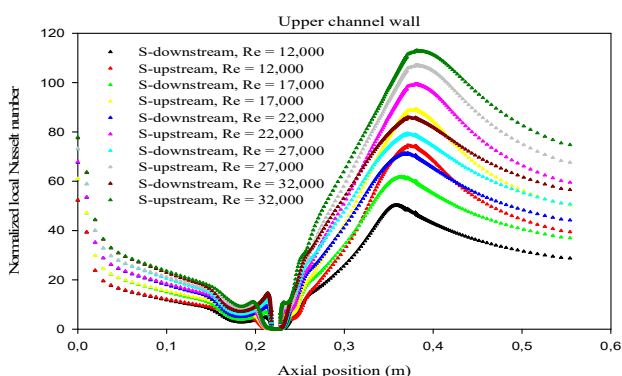


Fig. 13. Variation of normalized local Nusselt number along upper channel wall for various S-baffles and Reynolds numbers.

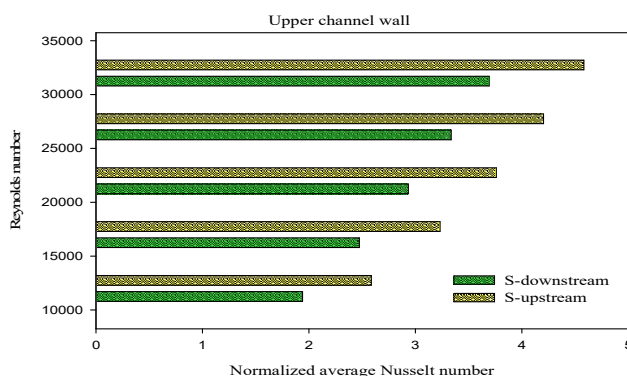


Fig. 14. Variation of normalized average Nusselt number with Reynolds number for various S-baffles.

The TEF values range from 1.326 in the case of S-upstream baffle for the lowest value of the Reynolds number (12,000) to 1.513 in the case of S-downstream for the maximum value of the Reynolds number (32,000). It is observed that the TEFs for the S-downstream baffle generally are found to be above the unity and to be much higher than those for employing the S-upstream baffle at similar flow conditions. This indicates that the use of the S-downstream baffle leads to the advantage over that of the S-upstream ones.

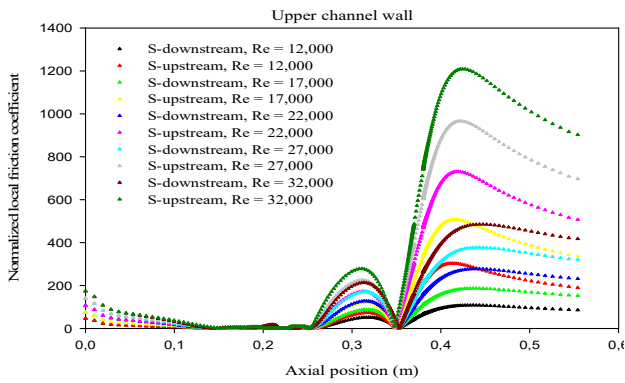


Fig. 15. Variation of normalized local friction coefficient along upper channel wall for various S-baffles and Reynolds numbers.

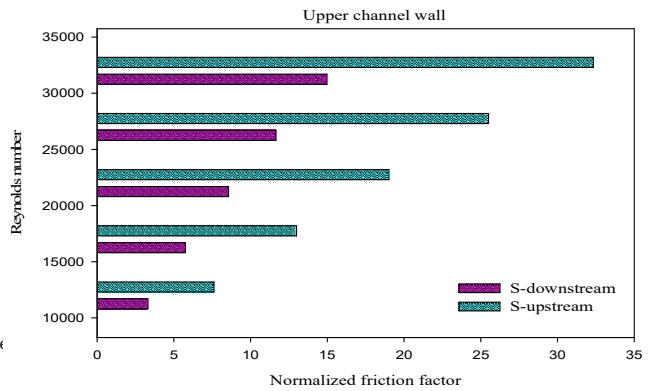


Fig. 16. Variation of normalized average friction coefficient with Reynolds number for various S-baffles.

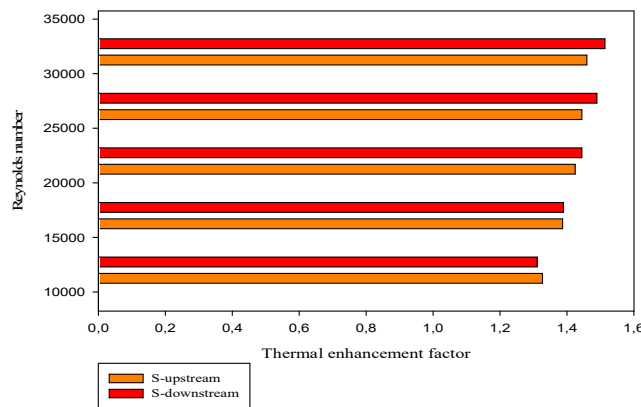


Fig. 17. Performance evaluation for both S-upstream and S-downstream baffles.

5. Conclusion

Through this simulation, an analysis was conducted to examine the thermal and aerodynamic fields of air inside a 2D horizontal rectangular section channel. Two transverse, staggered, S-shaped, solid-type baffles were inserted into the channel in order to develop vortices to improve the mixing, and consequently, the heat transfer. The steady-state turbulent flow equations were solved using the finite volume method. In particular, the contour plots of streamlines, the fields of velocity and temperature, the profiles of axial velocity, the normalized local and average coefficients of the skin friction, the normalized local and average numbers of Nusselt, and the factor of thermal enhancement were obtained and investigated numerically. The present numerical results in terms of the axial velocity and dynamic pressure profiles were compared with the experimental ones found in the literature. This comparison indicated that a qualitative agreement and a very good concordance exist between the two results. The results obtained in the present smooth rectangular channel agreed pretty well within the range of $\pm 3.5\%$ in comparison with Dittus-Boelter correlation (1930) for the Nu_0 and $\pm 1.15\%$ in comparison with Petukhov correlation (1970) for f_0 . Important deformations and large recirculation regions were observed in the flow field. Typically, the intensity of the vortices depended heavily on the functioning parameters of the S-model under consideration. It was widely admitted that their lengths are directly proportional to the Reynolds number. The present flow structure had significant influences on the temperature field distributions in the entire domain under investigation. The hottest regions were generally located in the neighborhood of the heated top surface and the tips of the S-baffle. The largest value of the axial variations of the Nusselt number and the skin friction coefficient was found in the region facing the second S-baffle, while the smallest value was in the region near the first S-baffle. The channel containing the S-obstacles with a large Reynolds number gave higher heat transfer, friction loss, and thermal enhancement factor than the one with a smaller Reynolds number. For using the S-baffles, it was observed that the TEFs for the S-downstream baffle generally are found to be above the unity and to be much higher than those for employing the S-upstream baffle at similar flow conditions. This indicated that the use of the S-downstream baffle leads to the advantage over that of the S-upstream ones. This simulation can be applied in improving the thermal efficiency of heat exchangers as well as solar air baffled channel collectors and electronic packages.

Finally, based on the present CFD analysis, several future developments are to be considered and the following research perspectives should be recommended:

- (i) Further studies are recommended to determine the best position of the 'S'-shaped baffle on the surfaces of the channel. The best geometry parameters of the channel, such as the size, width, thickness, inclination, etc, must be determined.
- (ii) New heat exchange surfaces should be considered by introducing perforated 'S'-shaped baffles. It is also advocated to deepen this study in order to determine the effects of several parameters, such as the porous medium permeability, the number



and the dimensions of pores, the Darcy number, and the thermal conductivity on thermal heat and fluid flow.

(iii) The rest of this research work could also be oriented towards three-dimensional modeling and simulation studies of the entire plane air solar collector.

Acknowledgments

This research was funded by the Research Unit of Materials and Renewable Energies, Abou Bekr Belkaid University, Republic of Algeria. The authors would like to thank Prof. Ali J. Chamkha for his suggestions.

Conflict of Interest

The authors declare no conflict of interest.

References

- [1] K.M. Kelkar, and S.V. Patankar, Numerical prediction of flow and heat transfer in a parallel plate channel with staggered fins, *J. Heat Transfer* 109 (1987) 25-30.
- [2] P.R. Mashaei, S.M. Hosseinalipour, N. Bagheri, M. Taheri-Ghazvini, and S. Madani, Simultaneous effect of staggered baffles and dispersed nanoparticles on thermal performance of a cooling channel, *Appl. Therm. Eng.* 120 (2017) 748-762.
- [3] S. Skullong, S. Kwankaomeng, C. Thianpong, and P. Promvonge, Thermal performance of turbulent flow in a solar air heater channel with rib-groove turbulators. *Int. Commun. Heat Mass Transfer* 50 (2014) 34-43.
- [4] C.B. Hwang, and C.A. Lin, A low Reynolds number two-equation $k\theta-\epsilon\theta$ model to predict thermal fields, *Int. J. Heat Mass Transfer* 42 (1999) 3217-3230.
- [5] A.S. Ambekar, R. Sivakumar, N. Anantharaman, and M. Vivekenandan, CFD simulation study of shell and tube heat exchangers with different baffle segment configurations, *Appl. Therm. Eng.* 108 (2016) 999-1007.
- [6] A.P. Rallabandi, N. Alkhamis, and J.C. Han, Heat transfer and pressure drop measurement for a square channel with 45 deg round-edged ribs at high Reynolds number, *Journal of Turbomachinery* 133(3) (2011) 031019.
- [7] M.A. Habib, A.M. Mobarak, M.A. Sallak, E.A.A. Hadi, and R.I. Affify, Experimental investigation of heat transfer and flow over baffles of different heights, *J. Heat Transfer* 116 (1994) 363-368.
- [8] H. Liu, and J. Wang, Numerical investigation on synthetical performances of fluid flow and heat transfer of semiattached rib-channels, *Int. J. Heat Mass Transfer* 54 (2011) 575-583.
- [9] T.M. Liou, and W.B. Wang, Laser holographic-interferometry study of developing heat-transfer in a duct with a detached rib array, *Int. J. Heat Mass Transfer* 38(1) (1995) 91-100.
- [10] C. Berner, F. Durst, and D.M. McEligot, Flow around baffles, *J. Heat Transfer* 106 (1984) 743-749.
- [11] P. Promvonge, T. Chompookham, S. Kwankaomeng, and C. Thianpong, Enhanced heat transfer in a triangular ribbed channel with longitudinal vortex generators, *Energy Convers. Manage* 51 (2010) 1242-1249.
- [12] J.C. Han, Y.M. Zhang, and C.P. Lee, Augmented heat transfer square channels with parallel, crossed, and V-shaped ribs, *J. Heat Transfer* 113 (1991) 590-596.
- [13] S. Acharya, S. Dutta, and T.A. Myrum, Heat transfer in turbulent flow past a surface-mounted two-dimensional rib, *J. Heat Transfer* 120(3) (1998) 724-734.
- [14] P. Promvonge, S. Sripattanapipat, S. Tamna, S. Kwankaomeng, and C. Thianpong, Numerical investigation of laminar heat transfer in a square channel with 45° inclined baffles, *Int. Commun. Heat Mass Transfer* 37 (2010) 170-177.
- [15] M. Mohammadi Pirouz, M. Farhadi, K. Sedighi, H. Nemati, and E. Fattahi, Lattice Boltzmann simulation of conjugate heat transfer in a rectangular channel with wall-mounted obstacles, *Sci. Iran. B* 18(2) (2011) 213-221.
- [16] P. Dutta, and A. Hossain, Internal cooling augmentation in rectangular channel using two inclined baffles, *Int. J. Heat Fluid Flow* 26 (2005) 223-232
- [17] Y.T. Yang, and C.Z. Hwang, Calculation of turbulent flow and heat transfer in a porous baffled channel, *Int. J. Heat Mass Transf.* 46(5) (2003) 771-780.
- [18] A. Tandiroglu, and T. Ayhan, Energy dissipation analysis of transient heat transfer for turbulent flow in a circular tube with baffle inserts, *Appl. Therm. Eng.* 26(2) (2006) 178-185.
- [19] H. Benzenine, R. Saim, S. Abboudi, and O. Imine, Numerical study on turbulent flow forced-convection heat transfer for air in a channel with waved fins, *Mechanics* 19(2) (2013) 150-158.
- [20] L.C. Demartini, H.A. Vielmo, and S.V Möller, Numeric and experimental analysis of the turbulent flow through a channel with baffle plates, *J. Braz. Soc. Mech. Sci. Eng.* 26(2) (2004) 153-159.
- [21] S. Kwankaomeng, and P. Promvonge, Numerical prediction on laminar heat transfer in square duct with 30° angled baffle on one wall, *Int. Comm. Heat Mass Transfer* 37(7) (2010) 857-866.
- [22] B. Peng, Q. W. Wang, C. Zhang, G. N. Xie, L. Q. Luo, Q. Y. Chen, and M. Zeng, An experimental study of shell-and-tube heat exchangers with continuous helical baffles, *J. Heat Transfer* 129 (2007) 1425-1431.
- [23] P. Stehlik, J. Nencansky, and D. Kral, Comparison of correction factors for shell-and-tube heat exchangers with segmental or helical baffles, *Heat Transfer Eng.* 15(1) (1994) 55-65.
- [24] Y. Menni, A. Azzi, Design and performance evaluation of air solar channels with diverse baffle structures, *Computational Thermal Sciences* 10(3) (2018) 225-249.
- [25] A. Abene, V. Dubois, M. Le Ray, and A. Ouagued, Study of a solar air flat plate collector: use of obstacles and application

- for the drying of grape, *J. Food Eng.* 65(1) (2004) 15-22.
- [26] F. Wang, J. Zhang, and S. Wang, Investigation on flow and heat transfer characteristics in rectangular channel with drop-shaped pin fins, *Propulsion and Power Research* 1(1) (2012) 64-70.
- [27] W. Jedsadaratanachai, N. Jayranaiwachira, and P. Promvonge, 3D numerical study on flow structure and heat transfer in a circular tube with v-baffles, *Chinese J. Chemical Eng.* 23 (2015) 342-349.
- [28] R. Kumar, R. Chauhan, M. Sethi, A. Sharma, and A. Kumar, Experimental investigation of effect of flow attack angle on thermohydraulic performance of air flow in a rectangular channel with discrete v-pattern baffle on the heated plate, *Advances Mech. Eng.* 8(5) (2016) 1-12.
- [29] S. Chamoli, and A. Taguchi, Approach for optimization of flow and geometrical parameters in a rectangular channel roughened with v down perforated baffles, *Case Studies Thermal Eng.* 5 (2015) 59-69.
- [30] C. Zamfirescu, and M. Feidt, Cascaded fins for heat transfer enhancement, *Heat Transfer Eng.* 28(5) (2007) 451-459.
- [31] M. Hosseini, D.D. Ganji, and M.A. Delavar, Experimental and numerical evaluation of different vortex generators on heat transfer, *Appl. Therm. Eng.* 108 (2016) 905-915.
- [32] A. Kumar, and M.H. Kim, Convective heat transfer enhancement in solar air channels, *Appl. Thermal Eng.* 89 (2015) 239-261.
- [33] S. Skullong, S. Kwankaomeng, C. Thianpong, and P. Promvonge, Thermal performance of turbulent flow in a solar air heater channel with rib-groove turbulators, *Int. Commun. Heat Mass Transfer* 50 (2014) 34-43.
- [34] S.V. Möller, L.A.M. Endres, and G. Escobar, Wall pressure field in a tube bank after a baffle plate, Transactions of SMIRT 15-15th Int. Conf. Structural Mechanics in Reactor Technology, Seoul, 7 (1999) 262-275.
- [35] I. Tanasawa, S. Nishio, K. Tanano, and M. Tado, Enhancement of forced convection heat transfer in a rectangular channel using turbulence promoters, Proc. of the ASME-USME Thermal Engineering Joint Conference (1983) 395-402.
- [36] Z.X. Yuan, W.Q. Tao, and Q.W. Wang, Numerical prediction for laminar forced convection heat transfer in parallel-plate channels with streamwise-periodic rod disturbances, *Int. J. Numerical Methods Fluids* 28 (1998) 1371-1387.
- [37] R. Kamali, and A.R. Binesh, The importance of rib shape effects on the local heat transfer and flow friction characteristics of square ducts with ribbed internal surfaces, *Int. Commun. Heat Mass Transfer* 35 (2008) 1032-1040.
- [38] C.H. Cheng, and W.H. Huang, Numerical prediction for laminar forced convection in parallel-plate channels with transverse fin arrays, *Int. J. Heat Mass Transfer* 34(11) (1991) 2739-2749.
- [39] J.R. Lopez, N.K. Anand, and L.S. Fletcher, Heat transfer in a three-dimensional channel with baffles, *Numerical Heat Transfer, Part A: Applications: An Int. J. Computation and Methodology* 30(2) (1996) 189-205.
- [40] S.S. Mousavi, and K. Hooman, Heat and fluid flow in entrance region of a channel with staggered baffles, *Energy Conversion and Management* 47(15) (2006) 2011-2019.
- [41] Y. Menni, A. Azzi, C. Zidani, Computational analysis of heat transfer and fluid flow characteristics over flat bars of different heights, *Revue des Energies Renouvelables* 19(3) (2016) 345-366.
- [42] P. Dutta, and S. Dutta, Effects of baffle size, perforation and orientation on internal heat transfer enhancement, *Int. J. Heat Mass Transfer* 4 (1998) 3005-3013.
- [43] D. Sahel, H. Ameur, R. Benzeguir, and Y. Kamla, Enhancement of heat transfer in a rectangular channel with perforated baffles, *Appl. Therm. Eng.* 101 (2016) 156-164.
- [44] P.R. Mashaie, M. Taheri-Ghazvini, R. Shabanpour Moghadam, and S. Madani, Smart role of Al₂O₃-water suspension on laminar heat transfer in entrance region of a channel with transverse in-line baffles, *Appl. Therm. Eng.* 112 (2017) 450-463.
- [45] S.S. Mousavi, and K. Hooman, Heat and fluid flow in entrance region of a channel with staggered baffles, *Energy Conversion and Management* 47(15) (2006) 2011-2019.
- [46] S. Sripattanapipat, and P. Promvonge, Numerical analysis of laminar heat transfer in a channel with diamond-shaped baffles, *Int. Comm. Heat Mass Transfer* 36(1) (2009) 32-38.
- [47] Nasiruddin, and M.K. Kamran Siddiqui, Heat transfer augmentation in a heat exchanger tube using a baffle, *Int. J. Heat Fluid Flow* 28(2) (2007) 318-328.
- [48] K. Torii, K.M. Kwak, and K. Nishino. Heat transfer enhancement accompanying pressure-loss reduction with winglet-type vortex generators for fin-tube heat exchangers, *Int. J. Heat Mass Trans.* 45 (2002) 3795-3801.
- [49] H.M. Yeh, and W.H. Chou, Efficiency of solar air heaters with baffles, *Energy* 16(7) (1991) 983-987.
- [50] T. Giovanni, Heat transfer in rectangular channels with transverse and V-shaped broken ribs, *Int. J. Heat Mass Trans.* 47 (2004) 229-243.
- [51] R. Bouchenafa, and R. Saim, Effect of position and height of a shield on convective heat transfer performances of plate fin heat sink, *Int. J. Numerical Methods Heat Fluid Flow* 25(5) (2015) 1047-1063.
- [52] M. Ghalambaz, E. Jamesahar, M.A. Ismael, and A.J. Chamkha, Fluid-structure interaction study of natural convection heat transfer over a flexible oscillating fin in a square cavity, *International Journal of Thermal Sciences* 111 (2017) 256-273.
- [53] H. Zargartalebi, A. Noghrehabadi, M. Ghalambaz, and I. Pop, Natural convection boundary layer flow over a horizontal plate embedded in a porous medium saturated with a nanofluid: case of variable thermophysical properties, *Transport in Porous Media* 107(1) (2015) 153-170.
- [54] A. Noghrehabadi, M. Ghalambaz, M. Ghalambaz, and A. Ghanbarzadeh, Comparing thermal enhancement of Ag-water and SiO₂-water nanofluids over an isothermal stretching sheet with suction or injection, *Journal of Computational and Applied Research in Mechanical Engineering* 2(1) (2012) 37-49.
- [55] A. Noghrehabadi, M. Ghalambaz, and A. Ghanbarzadeh, Heat transfer of magnetohydrodynamic viscous nanofluids over an isothermal stretching sheet, *Journal of Thermophysics and Heat transfer* 26(4) (2012) 686-689.

- [56] A. Noghrehabadi, R. Pourrajab, and M. Ghalambaz, Effect of partial slip boundary condition on the flow and heat transfer of nanofluids past stretching sheet prescribed constant wall temperature, *International Journal of Thermal Sciences* 54 (2012) 253-261.
- [57] A. Noghrehabadi, R. Mirzaei, M. Ghalambaz, A. Chamkha, and A. Ghanbarzadeh, Boundary layer flow heat and mass transfer study of Sakiadis flow of viscoelastic nanofluids using hybrid neural network-particle swarm optimization (HNNPSO), *Thermal Science and Engineering Progress* 4 (2017) 150-159.
- [58] M. Sabour, M. Ghalambaz, and A. Chamkha, Natural convection of nanofluids in a cavity: criteria for enhancement of nanofluids, *International Journal of Numerical Methods for Heat & Fluid Flow* 27(7) (2017) 1504-1534.
- [59] M. Ghalambaz, A. Doostani, E. Izadpanahi, and A.J. Chamkha, Phase-change heat transfer in a cavity heated from below: The effect of utilizing single or hybrid nanoparticles as additives, *Journal of the Taiwan Institute of Chemical Engineers* 72 (2017) 104-115.
- [60] B.E. Launder, and D.B. Spalding, The numerical computation of turbulent flows, *Computer Methods Applied Mechanics Eng.* 3 (1974) 269-289.
- [61] F. Incropera, and P.D. Dewitt, *Introduction to heat transfer*, fifth ed. John Wiley & Sons Inc., 2006.
- [62] S.V. Patankar, *Numerical heat transfer and fluid flow*, McGraw-Hill, New York, 1980.
- [63] B.P. Leonard, and S. Mokhtari, *Ultra-sharp nonoscillatory convection schemes for high-speed steady multidimensional flow*, NASA TM 1-2568, NASA Lewis Research Center, 1990.



© 2019 by the authors. Licensee SCU, Ahvaz, Iran. This article is an open access article distributed under the terms and conditions of the Creative Commons Attribution-Non Commercial 4.0 International (CC BY-NC 4.0 license) (<http://creativecommons.org/licenses/by-nc/4.0/>).